*Journal of the Meteorological Society of Japan*, **98**(4), 755−773, 2020. doi:10.2151/jmsj.2020-038

Special Edition on Global Precipitation Measurement (GPM): 5th Anniversary

# 4-year Climatology of Global Drop Size Distribution and its Seasonal Variability Observed by Spaceborne Dual-frequency Precipitation Radar

**Moeka YAMAJI**

*Earth Observation Research Center, Japan Aerospace Exploration Agency, Tsukuba, Japan*
*Department of Geography, Tokyo Metropolitan University, Hachioji, Japan*

**Hiroshi G. TAKAHASHI**

*Department of Geography, Tokyo Metropolitan University, Hachioji, Japan*

**Takuji KUBOTA, Riko OKI**

*Earth Observation Research Center, Japan Aerospace Exploration Agency, Tsukuba, Japan*

**Atsushi HAMADA**

*Faculty of Sustainable Design, University of Toyama, Toyama, Japan*

**and**

**Yukari N. TAKAYABU**

*Atmosphere and Ocean Research Institute, The University of Tokyo, Kashiwa, Japan*

*(Manuscript received 16 November 2019, in final form 6 April 2020)*

## Abstract

This study investigates the global drop size distribution (DSD) of rainfall and its relationship to large-scale precipitation characteristics using the Dual-frequency Precipitation Radar (DPR) onboard the Global Precipitation Measurement (GPM) Core Observatory. This study focuses on seasonal variations in the dominant precipitation systems regarding variations in DSD. A mass-weighted mean diameter ($D_m$), which is estimated based on the dual-frequency information derived from the GPM/DPR, is statistically analyzed as a typical parameter of the DSD. Values of the annual mean $D_m$, in general, are larger over land than over the oceans, and the relationship between $D_m$ and precipitation rate ($R$) is not a simple one-to-one relationship. Furthermore, $D_m$ exhibits statistically significant seasonal variations, specifically over the northwest Pacific Ocean, whereas $R$ shows insignificant variations, indicating the variations in $R$ cannot explain the distinct seasonal changes in $D_m$. Focusing on the seasonal variation in $D_m$ over the northwest Pacific Ocean, the results indicate that the variation in $D_m$ is related to the seasonal change in the dominant precipitation systems. In the summer over the northwest Pacific Ocean, $D_m$ is related to the organized precipitation systems associated with the Baiu front over the mid-latitudes and tropical disturbances over the subtropical region, with relatively higher precipitation top heights, composed of both stratiform and convective precipitations. Contrary to the summer, larger $D_m$ over the mid-latitudes in winter is related to extra-

Corresponding author: Moeka Yamaji, Earth Observation Research Center, Japan Aerospace Exploration Agency, 2-1-1 Sengen, Tsukuba, Ibaraki, 305-8505, Japan
E-mail: yamaji.moeka@jaxa.jp
J-stage Advance Published Date: 27 May 2020

©The Author(s) 2020. This is an open access article published by the Meteorological Society of Japan under a Creative Commons Attribution 4.0 International (CC BY 4.0) license (https://creativecommons.org/licenses/by/4.0).

tropical frontal systems with ice particles in the upper layers, which consists of more stratiform precipitation in the storm track region. The smaller $D_m$ over the subtropical northwest Pacific Ocean in winter is associated with shallow convective precipitation systems with trade-wind cumulus clouds and cumulus congestus under the subtropical high.

**Keywords** GPM; rainfall; precipitation system; seasonal change; precipitation characteristics

**Citation** Yamaji, M., H. G. Takahashi, T. Kubota, R. Oki, A. Hamada, and Y. N. Takayabu, 2020: 4-year climatology of global drop size distribution and its seasonal variability observed by spaceborne dual-frequency precipitation radar. *J. Meteor. Soc. Japan*, **98**, 755–773, doi:10.2151/jmsj.2020-038.

## 1. Introduction

Precipitation is essential for life; however, its distribution is not spatially homogeneous over the Earth, and many areas experience water shortages, droughts, and floods. To understand the criticality of precipitation in the water cycle, one must know the amount and characteristics of precipitation (IPCC 2014). One of the parameters that characterize precipitation is the drop size distribution (DSD), which is the number of drops per unit volume as a function of the drop diameter. DSD is a fingerprint of processes that could vary in precipitation systems as per the diurnal cycle, seasonal changes, and other environmental factors (e.g., Bringi et al. 2003; Kozu et al. 2006; Dolan et al. 2018). Furthermore, DSD is closely related to the formation of precipitation through microphysical processes for clouds and precipitation (Testud et al. 2001; Kozu et al. 2009). Regarding the remote sensing techniques, it is well known that DSD information is critical to retrieve precipitation by using ground radars because it determines the relationship between radar reflectivity ($Z$) and precipitation rate ($R$) (Marshall and Palmer 1948). However, DSD is still a highly uncertain factor in these fields (Wang et al. 2010), thus requiring a detailed investigation of DSD.

Previous studies investigated the local characteristics of DSD via ground-based observations (e.g., Bringi et al. 2003; Kozu et al. 2006; Dolan et al. 2018). They found that DSD depends on factors such as precipitation type (convective or stratiform) and local climatological regimes. For instance, Kozu et al. (2006) investigated the diurnal and seasonal variations in DSD at three locations with different climates (Gadanki in India, Singapore, and Kototabang in Indonesia) by using ground-based measurements. They showed that diurnal convective cycles and seasonal variations in precipitation affected DSD. Furthermore, the amplitude of DSD variations was unique to each location. The seasonal variation was significant in Gadanki, whereas the diurnal variation was large in Kototabang. Singapore exhibited smaller seasonal and diurnal variations due to the oceanic effect. They concluded that DSD characteristics were associated with the dominant local precipitation systems.

Previous studies often used ground-based observation of DSD from disdrometers and dual-polarimetric meteorological radars. Disdrometers can provide DSD information at a specific site with a high temporal resolution, such as particle size velocity (PARSIVEL) disdrometers measuring droplet size and fall velocity (Löffler-Mang and Joss 2000), and 2D video disdrometers (2DVD) measuring the size, fall velocity, and shape of each drop (Kruger and Krajewski 2002). Dual-polarimetric meteorological radars provide the spatial distribution of drop size information within a specific region by assuming DSD models (Ulbrich 1983; Straka et al. 2000; Brandes et al. 2004). A modified gamma distribution with three parameters is often adopted, as defined in Eq. (1):

$$N(D) = N_0 D^{\mu} \exp(-\Lambda D) = N_w f(\mu) D^{\mu} \exp\left(-\frac{(4+\mu)}{D_m} D\right), \quad (1)$$

where $D$ denotes the diameter of a precipitation particle; $N(D)$, the number density; and $N_w$, $N_0$, $\mu$, and $\lambda$, the DSD parameters.

Recently, Dolan et al. (2018) conducted a statistical analysis using long-term disdrometer records from high-, middle-, and low-latitude regions and found that the DSD varied with latitude. This result suggests that DSDs reflect the characteristics of dominant precipitation systems in each latitudinal band. Specifically, deep convection and warm cloud depths with robust coalescence processes were dominant over the low latitudes, whereas weak convections were dominant over the high latitudes. In the mid-latitudes, the

stratiform systems with a clear bright band signature and larger melted ice particles were dominant. Even though longer DSD data records enable such statistical analysis, ground-based observations are still spatially limited.

In addition to the ground-based DSD measurements, spaceborne precipitation radars can provide DSD information that should be another source of information for understanding large-scale DSD characteristics. The Tropical Rainfall Measuring Mission (TRMM) satellite was launched in 1997 (Kummerow et al. 1998; Kozu et al. 2001) and carried the Precipitation Radar (PR) with a frequency in the Ku-band. The TRMM/PR provided DSD information based on the single-frequency estimation method for more than 17 years (Iguchi et al. 2000, 2009). Following the success of the TRMM, the Global Precipitation Measurement (GPM) Core Observatory was launched in 2014 (Kojima et al. 2012; Hou et al. 2014; Skofronick-Jackson et al. 2017).

GPM has two major advantages over TRMM, namely, a dual-frequency radar observation and a broader observation area, including mid-latitudes. The Dual-frequency Precipitation Radar (DPR) consists of the Ku-band precipitation radar (KuPR) and the Ka-band precipitation radar (KaPR). The DPR delivers dual-frequency retrievals of two DSD parameters based on the differential scattering properties of precipitation particles at these two frequencies. Recently, Iguchi et al. (2018) developed an algorithm for detecting heavy ice precipitation by using the differential scattering properties obtained from GPM/DPR. Akiyama et al. (2019) conducted a case study to investigate the heavy ice precipitation band in an oceanic cyclone observed by GPM/DPR. Thus, the GPM/DPR allows a more accurate global estimation of rainfall particle information than the TRMM/PR with its single-frequency measurement. Seto et al. (2016) reviewed the DSD information derived from the GPM/DPR algorithm, including the differences between the KuPR-only algorithm and the DPR algorithm. They revealed that the dual-frequency method could work more effectively to adjust DSD parameters from assumed basic DSD models by using dual-frequency information, even in a weak precipitation range, where the single-frequency method did not work well. As an applicational study of DSD by GPM/DPR, Radhakrishna et al. (2020) revealed the regional differences in DSD over the Indian region by using GPM/DPR and found that the characteristics of DSD were different, depending on climatic fields.

Furthermore, the GPM Core Observatory has a higher orbital inclination (65°) than the TRMM (35°), and it realized the world's first precipitation observation by spaceborne PR over the mid-latitudes. Kobayashi et al. (2018) examined the vertical gradient of radar reflectivity below the bright band from tropics to mid-latitudes using KuPR onboard the GPM Core Observatory. They found differences in the vertical profiles of radar reflectivity for stratiform precipitation between the tropics and mid-latitudes. Therefore, expanding the observation area of the GPM Core Observatory enables us to investigate large-scale distributions of DSD and precipitation seamlessly from the tropics to mid-latitudes.

This study aimed to observe the global distribution of the mean drop size and its relationship to large-scale distributions of precipitation characteristics using 4 years of the GPM/DPR observations, which provide more accurate DSD information than the TRMM/PR. In particular, the authors provide information about the drop size over oceans for the first time using the GPM/DPR observations. This study also focuses on seasonal variations.

Section 2 provides the datasets and methodology used in this study. The results are presented in Section 3, including the results of the 4-year climatology and seasonal differences. Section 4 provides the results focusing on the northwest Pacific Ocean and comparison with precipitation characteristics, and Section 5 discusses the possible association between DSD characteristics and dominant precipitation systems. The pixel-based analysis to confirm the $R$–$D_m$ relationship is explained in Section 6, and Section 7 provides the conclusions.

## 2. Data and methodology

### *2.1 GPM/DPR observations*

To investigate large-scale DSD distributions, this study used 4 years of data (from June 2014 to May 2018) from the GPM/DPR Level-2 Version 05 products (Iguchi et al. 2017). The GPM/DPR algorithm can be divided into the KuPR-only algorithm, the KaPR-only algorithm, and the dual-frequency algorithm (using both KuPR and KaPR) (Seto et al. 2013; Seto and Iguchi 2015; Seto 2019). This study used the DPR Level-2 (DPRL2) product with the dual-frequency algorithm. The DPR algorithm assumes that the DSD follows the modified gamma distribution, as described in Eq. (1), where $\mu$ is set to 3, and two unknown parameters are obtained from the GPM/DPR observations. $R$ in mm h$^{-1}$ can be interpreted as a DSD parameter because it is a function of DSD parameters if the terminal fall speed is given. The DPRL2

algorithm uses $R$ and $D_m$, as presented in Eq. (2) for stratiform and Eq. (3) for convective, respectively:

$$R = 0.401\varepsilon^{4.649} D_m{}^{6.131} \text{ (for stratiform)}, \quad (2)$$

$$R = 1.370\varepsilon^{4.258} D_m{}^{5.420} \text{ (for convective)}. \quad (3)$$

The units of $R$ and $D_m$ are mm $h^{-1}$ and mm, respectively. Here, $\varepsilon$ is an adjustment factor. In the dual-frequency algorithm, the dual-frequency surface reference technique (Meneghini et al. 2015) and KaPR's $Z$ are used to adjust $\varepsilon$ (Seto 2019). The $R$–$D_m$ relationship in the GPM/DPR algorithm in Eqs. (2) and (3) is derived from the same set of DSD measurements (Kozu et al. 2009), which was also used in the $Z$–$R$ relationship in the TRMM/PR algorithm. $\varepsilon$ is defined by different methods for TRMM/PR with single-frequency radar (Iguchi et al. 2000, 2009) and for the GPM/DPR with dual-frequency radar (Seto et al. 2013; Seto and Iguchi 2015; Seto 2019).

This study focuses on $D_m$ at the near surface (clutter-free bottom) as a typical parameter of the DSD and shows a 4-year annual mean global distribution of $D_m$. Data are averaged onto a 2.5° × 2.5° box (latitude and longitude) in two steps to ensure that the seasonal characteristics are not missed. In the first step, we average values seasonally, in other words, every 3 months (March–April–May (MAM), June–July–August (JJA), September–October–November (SON), and December–January–February (DJF)) from an orbit-based level-2 product (e.g., 2014JJA, 2014SON, and so on). If the number of observation samples of the level-2 product in a 2.5° × 2.5° box is less than 64 in the first step, the 2.5° × 2.5° box is treated as missing. Note that the number 64 for the selection threshold was also chosen in a previous study using the TRMM data (Kozu et al. 2009). In the second step, a 3-month dataset is taken as one sample, and the 4-year annual mean is calculated. If the number of non-missing 3-month $D_m$ data in each season is more than 3 (the maximum value is 4 as the total duration of 4 years), the grid box is plotted. The target domain is 65°N–65°S. The DPRL2 products include phase information, such as liquid, mixed, or solid, using vertical profiles of radar reflectivity and ancillary atmospheric environmental data, such as temperature.

This study focuses on $D_m$ in the liquid phase as a first step to investigate the DSD information obtained by the GPM/DPR, so that the mixed and solid phases at the clutter-free bottom are excluded and that only data in the liquid phase at the clutter-free bottom are analyzed. In addition to $D_m$, the 4-year annual mean global distribution of $R$ is also calculated and compared with that of $D_m$. It is noted that the averages of $R$ and $D_m$ are obtained only when precipitation in the form of liquid water (rain) is present at the near surface gate.

The 3-month mean (MAM, JJA, SON, and DJF) distributions of $D_m$ and $R$ are calculated from the DPRL2 product to investigate seasonal differences. The treatment of missing values is the same as that for the annual mean. To determine the difference between JJA and DJF, Welch's $t$ test (Welch 1938) is conducted to detect statistically significant differences with a 99 % confidence level by taking a 3-month mean for a year as one sample.

Furthermore, precipitation top heights, stratiform ratio, and ratio of pixels with heavy ice precipitation are analyzed to capture the characteristics of precipitation. Precipitation top heights are defined as the highest altitude where the precipitation rate is above 0.3 mm $h^{-1}$. The threshold of 0.3 mm $h^{-1}$ is set by considering the sensitivity of the DPR instrument (Kojima et al. 2012). The stratiform ratio is defined as the ratio of pixels identified as stratiform to the total number of rain-conditioned pixels. The type classification of precipitation (i.e., convective, stratiform, or other) is as defined in the DPRL2 algorithm. The flagHeavyIcePrecipitation (flagHIP) in DPRL2 products is used to calculate the ratio of pixels with heavy ice precipitation. The measured dual-frequency ratio ($DFR_m$) and measured apparent radar reflectivity factor ($Z_m$) by KuPR are used to detect heavy ice precipitation. The detailed algorithm is described by Iguchi et al. (2018).

The pixel-by-pixel $R$–$D_m$ relationship at a clutter-free bottom is investigated using DPRL2 products to elucidate whether a change in $R$, a change in the characteristics of the precipitation, or a combination of both causes the seasonal variation in $D_m$.

It should be noted that this study aimed to characterize the large-scale variations in $D_m$, and that evaluating the accuracy of the DSD product by the GPM/DPR data is beyond the scope of this study. Previous studies validated the DSD product of the GPM/DPR against ground-based observation networks (Petersen 2017; Petersen et al. 2018; D'Adderio et al. 2018). They revealed that the specific GPM science requirement of $D_m$ to within +/−0.5 mm of ground-based observation is satisfied overall in the DPR Version 05 dataset. Moreover, the relationship between $D_m$ observed through ground validation and $D_m$ from the DPR is statistically significant, despite biases in the products. This allows a discussion not about the absolute values of $D_m$ but about the statistically significant differences of $D_m$ over the seasonal cycle. This study

extends the findings regarding seasonal differences of DSD that Kozu et al. (2009) revealed by using the TRMM/PR to the mid-latitudes by using the GPM/DPR.

### 2.2 *Atmospheric reanalysis dataset*

In addition to the GPM/DPR observations, atmospheric reanalysis data are used to discuss the dominant precipitation systems. Horizontal winds at the 850 hPa level and sea level pressure (SLP) from the Japanese 55-year reanalysis, known as JRA-55 (Kobayashi et al. 2015), are used. This dataset enables investigations of the dominant atmospheric circulations, which are analyzed independently from the GPM/DPR dataset. The resolution of the JRA-55 is 1.25° × 1.25° at 6-h intervals.

The 3-month mean distributions of horizontal winds at 850 hPa and SLP are calculated to quantify the seasonal differences in the atmospheric environment. Furthermore, composite analysis is conducted for horizontal winds using the JRA-55 to extract typical atmospheric circulations associated with the precipitation events. When the ratio of precipitating pixels to observing pixels by GPM/DPR in a certain area is more than 10 %, the JRA-55 sample at the nearest time is composited, as will be shown later in Section 4. The anomaly of the composite mean from the total mean was calculated and discussed.

## 3. Large-scale distribution of $D_m$ and its seasonal variations

### 3.1 *Global distribution of* $D_m$

Figure 1a presents the 4-year annual mean of $D_m$ in mm at the clutter-free bottom, showing that $D_m$, in general, is larger over land than over the oceans. Notably, large-scale distributions of $D_m$, including mid-latitudes, are newly obtained by the GPM/DPR observation.

As explained in Section 1, $D_m$ is closely related to the formation of precipitation through microphysical processes for clouds and precipitation, and it reflects precipitation characteristics, such as the diurnal cycle and seasonal changes. The regional characteristics of $D_m$ are reviewed by considering those of $R$ in this subsection because $R$ is the most fundamental parameter for characterizing precipitation and is closely related to $D_m$, as expressed in Eqs. (2) and (3). If ε has a constant value, $D_m$ should correspond to $R$ with a one-to-one relationship, as understood in Eqs. (2) and (3), even though there are differences between stratiform and convective precipitations. In practice, since the values of ε depend on precipitation characteristics, the actual mean $D_m$ does not completely correspond to mean $R$.

Figure 1b presents the 4-year annual mean of conditional $R$ in mm $h^{-1}$ at the clutter-free bottom. Comparing $D_m$ in Fig. 1a with $R$ in Fig. 1b, it is found that the relationship is not a simple one-to-one relationship, suggesting a more complicated relationship between precipitation and liquid droplet size.

Over land, a larger mean $D_m$ corresponds to a larger mean $R$ around the Meghalaya region in the Indian subcontinent, the coastal area of the Gulf of Guinea and the Congo Basin on the African Continent, the Mississippi River coast in the North American Continent, and the La Plata River in the South American Continent. The results suggest that larger liquid raindrops are associated with stronger precipitation in these regions. Over tropical and subtropical oceans, a larger $D_m$ corresponds to a larger $R$ around the warm pool. A smaller $D_m$ corresponds to a smaller $R$ over and around the eastern parts of the oceans, which has cold sea surface temperature over the California Current and the Peru Current in the Pacific Ocean, the West Australian Current in the Indian Ocean, and the Benguela Current in the Atlantic Ocean.

Focusing on the Pacific Ocean, the relationship between $D_m$ and $R$ seems to be more complicated. For example, over the Intertropical Convergence Zone (ITCZ), $D_m$ does not have a homogeneous spatial distribution, whereas $R$ is homogeneously larger over the entire ITCZ region. Along the ITCZ in 5–15°N, the relationship between $R$ and $D_m$ is different in the equatorial central Pacific (120–150°W) from those in the surrounding regions. $D_m$ is smaller over the equatorial central Pacific, whereas it is larger over the equatorial eastern Pacific (130–180°E) and the western Pacific (90–120°W). This is consistent with the findings of Shige et al. (2008) who suggested that raindrops over the central Pacific (5–15°N, 120–150°W) were smaller than those over the western Pacific (2.5–12.5°N, 130–160°E).

As for the South Pacific Convergence Zone, $D_m$ is smaller, despite $R$ being larger over the subtropical region (30–15°S). Contrary to the subtropical high-pressure zone (15–30°N, 30–15°S), $D_m$ is larger, whereas $R$ is not so large over the oceans in the mid-latitudes (50–60°N, 60–30°S). The combination of a larger $D_m$ and a moderate $R$ is apparent, especially in the southern hemisphere where storm tracks are dominant all year round. The results over the entire mid-latitude region are newly identified in this study by using GPM/DPR. In this manner, we can find various regional characteristics of $D_m$, even though $R$

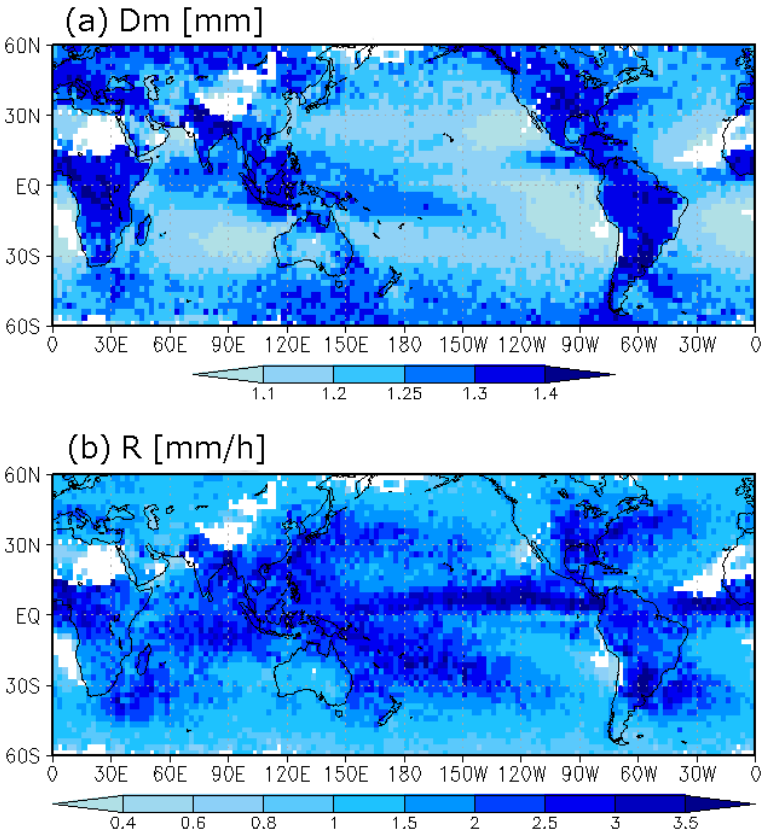


Fig. 1. 4-Year annual mean value (conditional) of (a) $D_m$ in mm and (b) $R$ in mm $h^{-1}$ at the clutter-free bottom level derived by DPRL2.

is similar, which could be associated with the climate regime and/or dominant precipitation systems.

### 3.3 *Seasonal differences of $D_m$*

The regional characteristics of the seasonal mean $D_m$ could be interpreted much clearer if we consider seasonal variations in precipitation characteristics. We compared the annual mean $D_m$ with the annual mean $R$ in the previous subsection and found that their relationship is not simple. In this subsection, we investigate the seasonal differences of mean $D_m$ regarding mean $R$. Figures 2a–d and 2e–h present 3-month mean anomalies from the 4-year annual mean $D_m$ and $R$, respectively. Over land in the Asian monsoon region with a drastic seasonal variation in $R$, $D_m$ in MAM is larger, whereas $D_m$ in JJA and DJF is smaller. The larger $D_m$ in MAM can be associated with the heavy precipitation in the pre-monsoon season, whereas the smaller $D_m$ in JJA is observed in the mature monsoon season, indicating the association with the seasonal changes in precipitation characteristics and dominant precipitation systems (Takahashi 2016; Ono and Takahashi 2016). Over the Amazon, $D_m$ is larger in JJA and SON, corresponding to a mainly dry season, whereas $D_m$ is smaller in DJF and MAM, corresponding to a mainly wet season (Collischonn et al. 2008). Over the oceans, distinct seasonal changes in $D_m$ are observed, specifically in JJA and DJF, although the seasonal changes cannot be explained by those of $R$. Larger $D_m$ in the summer hemisphere is found in the subtropics, and that in the winter hemisphere is found in the mid-latitudes, particularly over the Pacific Ocean.

Figure 3 presents the seasonal differences in $D_m$ (Fig. 3a) and $R$ (Fig. 3b) between JJA and DJF. In Fig. 3, the grid boxes with a statistically significant difference are identified using a statistical test. Clear seasonal differences are observed in $D_m$ over the mid-latitude Pacific Ocean (30–50°N/S) and the subtropical northern Pacific Ocean (10–30°N). Conversely, there are no obvious or systematic seasonal differences in $R$ in these regions. Note that there are also some organized signals in $D_m$ over the Atlantic

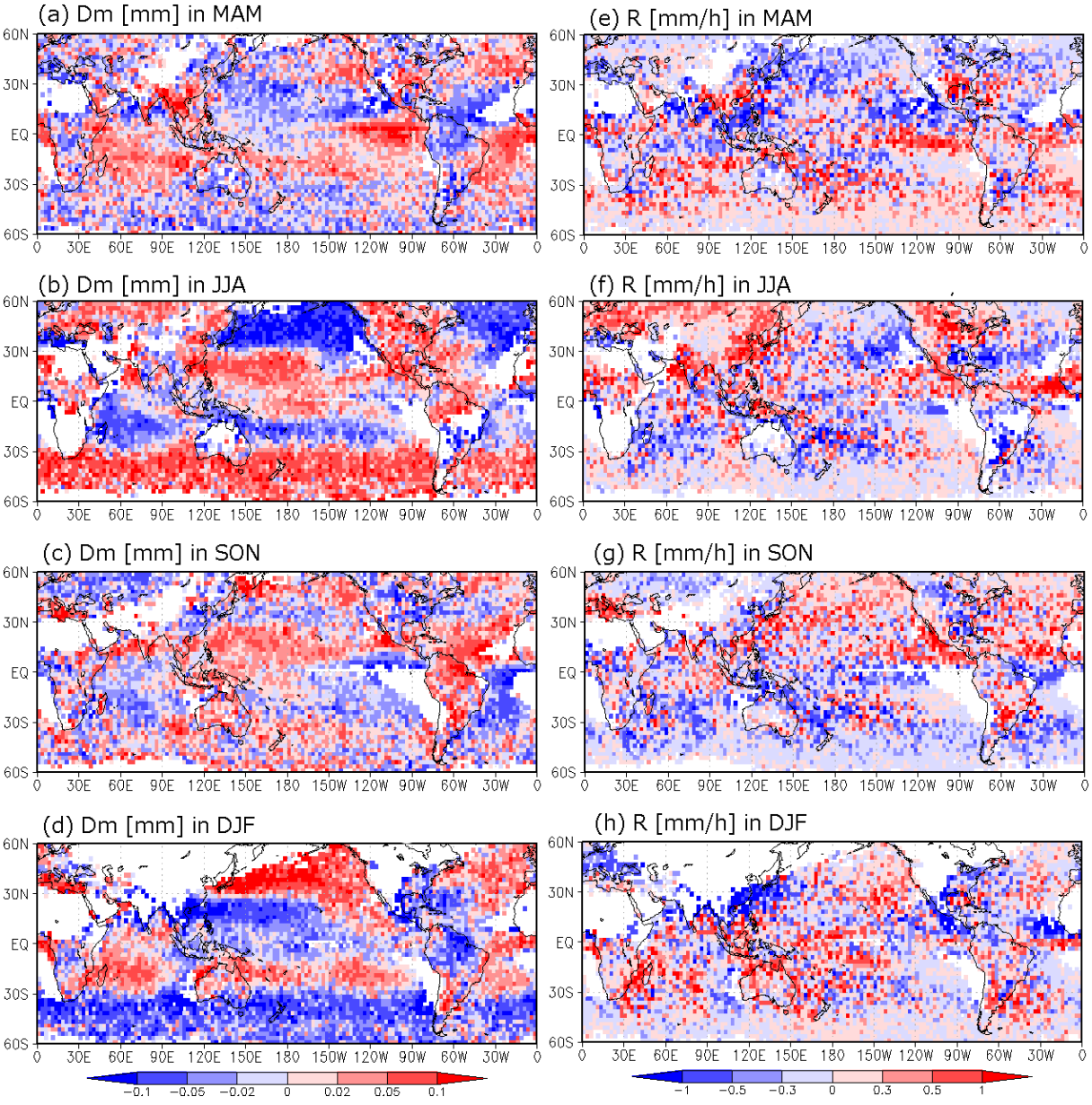


Fig. 2. 3-Month mean (conditional) anomalies from 4-year annual mean (conditional) of (a–d) $D_m$ in mm and (e–h) $R$ in mm h$^{-1}$ for (a, e) MAM, (b, f) JJA, (c, g) SON, and (d, h) DJF.

Ocean and the Indian Ocean. Region A over the mid-latitudes (30–50°N, 150°E–150°W) and Region B in the subtropics (10–30°N, 130°E–170°W) are extracted based on the seasonal changes in $D_m$ (Fig. 3a) for a detailed investigation in the following sections.

As mentioned previously, the GPM can observe rainfall and DSD over a broader area, including the mid-latitudes, using a dual-frequency radar. The seasonal variations in DSD information over tropical and subtropical regions were also estimated by the TRMM/PR (Kozu et al. 2009); these results were consistent with those of the current study. However, the orbital inclination of the TRMM was insufficient to determine the rainfall characteristics in the mid-latitudes. Clear seasonal variations in DSD information, including mid-latitudes, are newly detected by

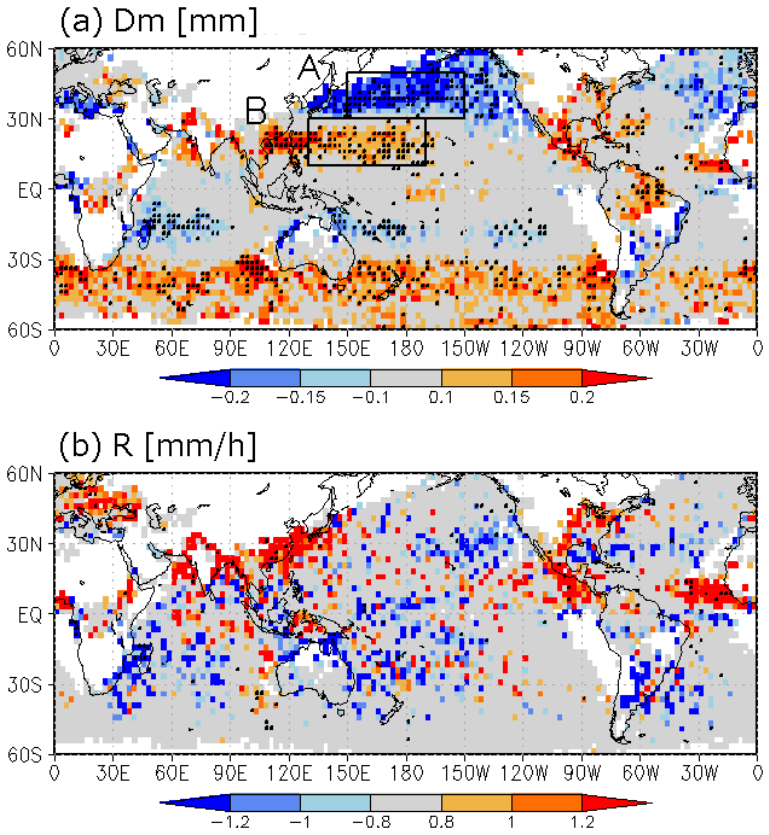


Fig. 3. Seasonal differences (JJA minus DJF) for (a) $D_m$ in mm and (b) $R$ in mm h$^{-1}$. The black dots indicate the boxes with statistically significant difference at a 99 % confidence level using Welch's $t$ test. The black open squares in Fig. 3a indicate Region A (30–50°N, 150°E–150°W) and Region B (10–30°N, 130°E–170°W) focused on in this study.

the GPM/DPR observations. A detailed analysis is conducted and discussed in the following sections, focusing on the northwest Pacific Ocean where the variation in $D_m$ is statistically significant.

## 4. Seasonal difference of $D_m$ and precipitation characteristics over the northwest Pacific Ocean

As presented in Figs. 2 and 3, significant seasonal variations in $D_m$ are observed over the subtropical and mid-latitude bands of the northwest Pacific Ocean between JJA and DJF. Figure 4 presents the 3-month mean values of $D_m$ (Figs. 4a, b), $R$ (Figs. 4c, d), precipitation top heights (Figs. 4e, f), and stratiform ratio (Figs. 4g, h) to outline the precipitation characteristics. As presented in Figs. 2 and 3, $D_m$ exhibits clear contrasts between Regions A and B, whereas $R$ does not. Conversely, precipitation characteristics, such as precipitation top heights in DJF and stratiform ratio in both JJA and DJF, differ across the boundary of 30°N, which is similar to the spatial pattern of seasonal differences in $D_m$. Figures 4e and 4f show that precipitation top heights are higher in JJA and lower in DJF, especially over the subtropical region. As for the stratiform ratio (Figs. 4g, h), precipitation is more stratiform over the mid-latitudes than over the subtropical region. This is consistent with the findings of Yokoyama et al. (2017, 2019), who characterized the mid-latitude-type precipitation with a stratiform precipitation ratio of over 80 % using the TRMM/PR Level-2 dataset. Moreover, a latitudinal contrast in stratiform ratios of the subtropical and mid-latitude regions seems larger over the northwest Pacific Ocean in DJF than in JJA.

These results indicate that the precipitation systems over the northwest mid-latitude Pacific region (Region A) consist of both stratiform and convective precipitations with high precipitation top heights in JJA, whereas the features change to more stratiform

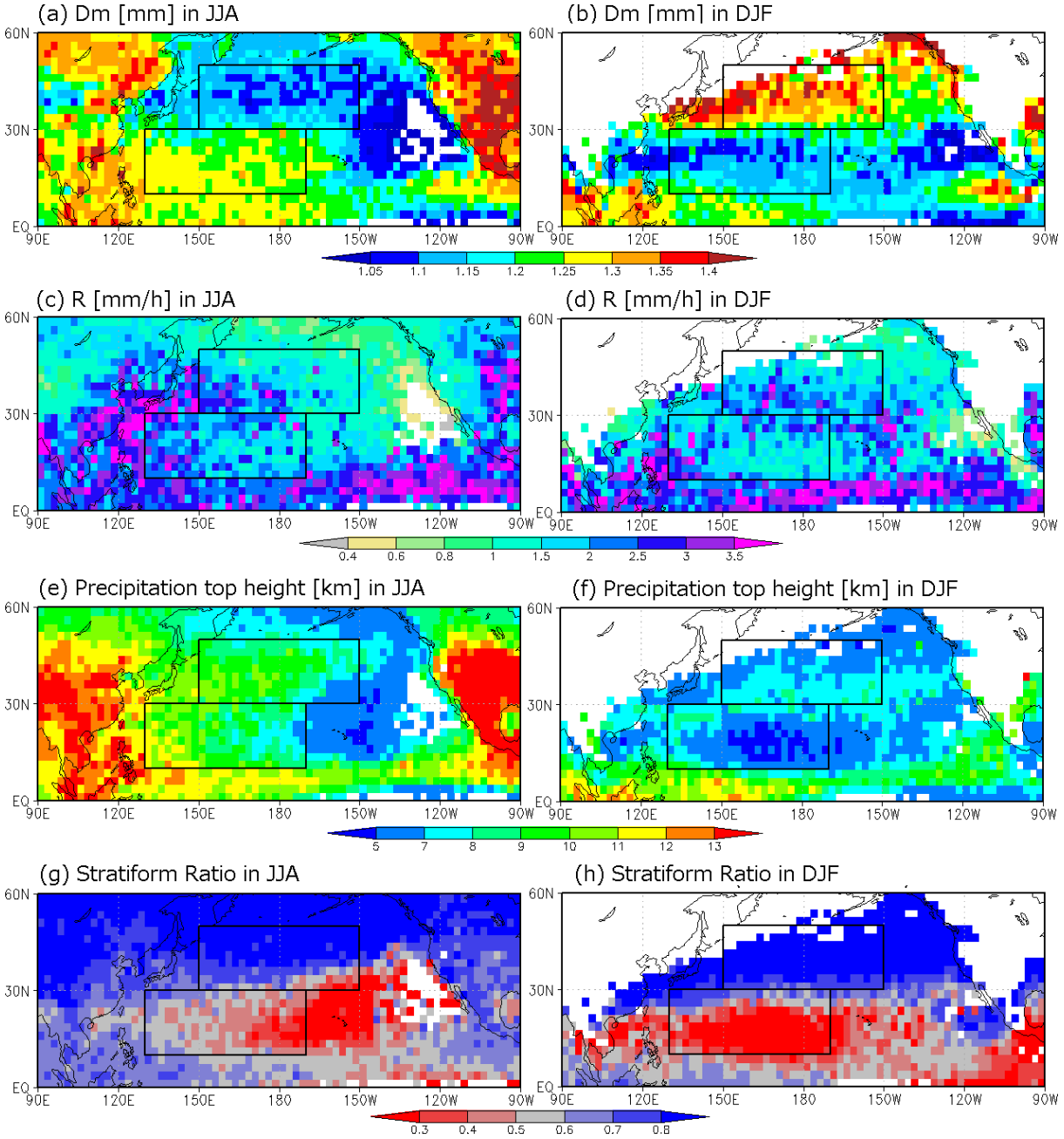


Fig. 4. 3-month mean value of (a–b) $D_m$ in mm, (c–d) $R$ in mm h$^{-1}$, (e–f) precipitation top heights in km, and (g–h) stratiform ratio. (a), (c), (e), and (g) and (b), (d), (f), and (h) are for JJA and DJF, respectively. The black open squares indicate Regions A and B, which are the same as in Fig. 3.

precipitation with moderate precipitation top heights in DJF. On the other hand, in the northwest subtropical Pacific region (Region B), precipitation systems in JJA consist of both stratiform and convective precipitations with high precipitation top heights, whereas those in DJF consist of more convective precipitation with lower precipitation top heights. Overall, the seasonal changes in precipitation characteristics, such as precipitation top heights and stratiform ratio, seem to relate to changes in $D_m$.

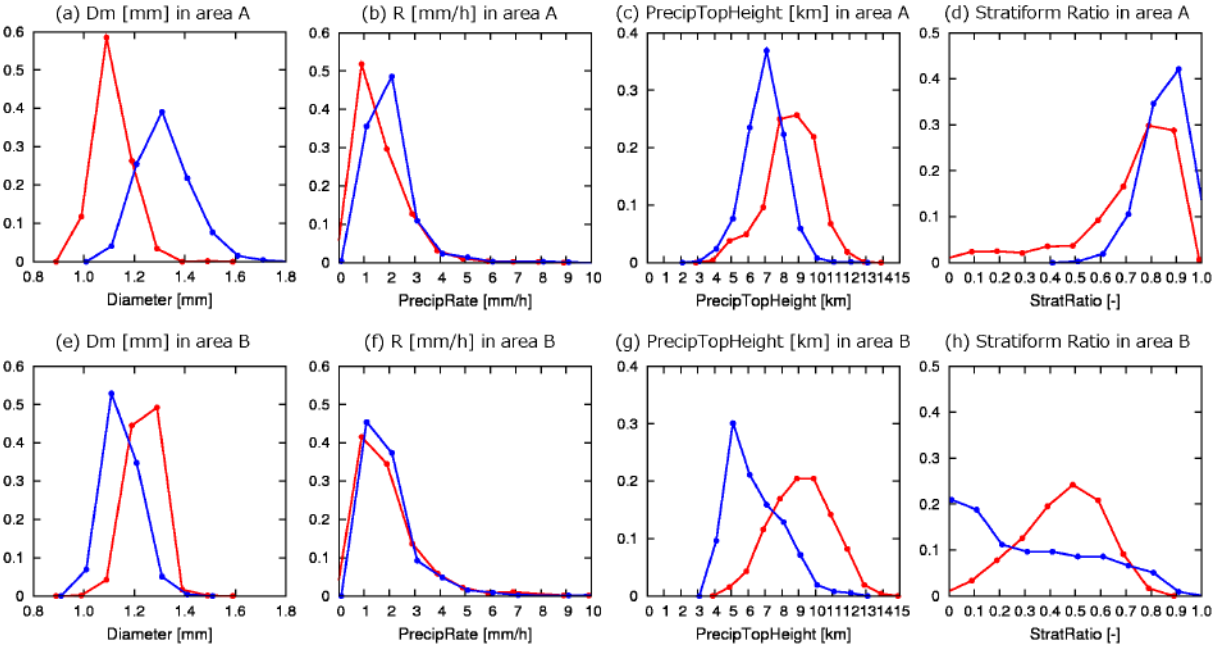


Fig. 5. Relative frequency of (a–d) Region A and (e–h) Region B of (a, e) $D_m$ in mm, (b, f) $R$ in mm h$^{-1}$, (c, g) precipitation top heights in km, and (d, h) stratiform ratio. Red and blue indicate the values in JJA and DJF, respectively.

Figure 5 presents the relative frequency of 3-month mean values for $D_m$, $R$, precipitation top heights, and stratiform ratio over Regions A and B for quantitative investigation. One sample corresponds to a 2.5° × 2.5° box for 3 months in a specific year. There are differences in peak values and/or shapes of the histogram for $D_m$, precipitation top heights, and stratiform ratio between JJA and DJF, although differences are not as evident for $R$.

In the mid-latitudes of Region A, the peak values of $D_m$ are 1.1 mm in JJA and 1.3 mm in DJF (Fig. 5a), whereas the peak values of $R$ are 1–2 mm h$^{-1}$ in both JJA and DJF (Fig. 5b). The dominant precipitation top height is 6–8 km in DJF, whereas it is 8–10 km in JJA (Fig. 5c). The range of relative frequency of the stratiform ratio is broad (from 0 to 1) in JJA; however, it is limited from 0.5 to 1.0 with high peaks at 0.8 and 0.9 in DJF (Fig. 5d). Therefore, both stratiform and convective precipitations exist in JJA, whereas stratiform precipitation is more dominant in DJF.

In Region B over the subtropics, the peak values of $D_m$ were 1.2–1.3 mm in JJA and 1.1 mm in DJF (Fig. 5e). However, $R$ has peak values of 1–2 mm h$^{-1}$ in both JJA and DJF (Fig. 5f), which is almost the same as in Region A. The peak range of relative frequency of precipitation top height is broad (from 8 to 11 km) in JJA, whereas approximately 60 % of the total samples are below 6 km in DJF (Fig. 5g). The range of relative frequency of the stratiform ratio is broad in JJA, whereas stratiform precipitation is much less dominant in DJF (Fig. 5h).

The results in Figs. 2 and 3 indicate that the seasonal mean values of $D_m$ vary significantly, whereas those of $R$ do not. The results in Figs. 4 and 5 support the possibility that seasonal and regional differences of $D_m$ could be related to the dominant precipitation systems due to the changing precipitation characteristics because the precipitation top heights and stratiform ratio varied regionally and seasonally regarding $D_m$.

## 5. Discussion of possible precipitation regimes corresponding to $D_m$ variations

This section discusses possible precipitation regimes, focusing on Regions A and B in JJA and DJF, respectively.

### *5.1 Organized precipitation systems over the subtropics and mid-latitudes in JJA*

For both Regions A and B in JJA, the precipitation top heights are high, and both stratiform and convective precipitations exists. These features are consistent with those for organized systems, such as squall lines,

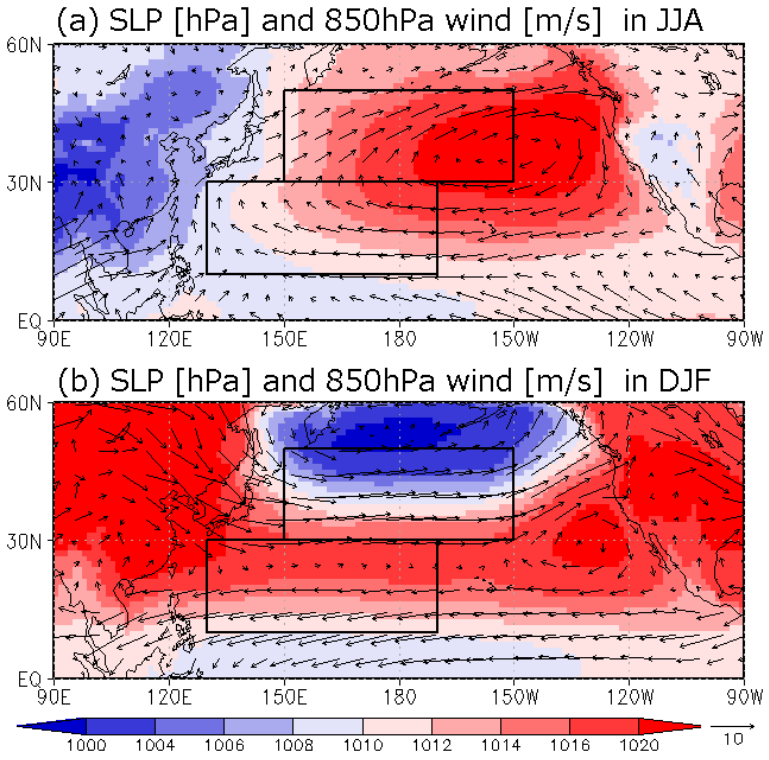


Fig. 6. 3-month mean distribution of SLP in hPa and horizontal winds at 850 hPa in m $s^{-1}$ for (a) JJA and (b) DJF calculated from JRA-55. The black open squares indicate Regions A and B, which are the same as in Fig. 3.

as expressed by Takayabu (2008) and Yokoyama et al. (2017, 2019). Houze (1977) investigated organized squall line systems using the observational network of the Global Atmospheric Research Program's Atlantic Tropical Experiment (GATE). The author suggested that an organized squall line consists of discrete active centers of cumulonimbus convection and stratiform anvils, and the maximum cloud tops reached heights of 16–17 km along the squall line. The characteristics of the JJA precipitation, such as tall precipitation top heights and the existence of both stratiform and convective precipitations, are consistent with those of organized precipitation systems that are described by Houze (1977) as squall lines and cloud clusters.

Figure 6 presents SLP and winds at 850 hPa in JJA (Fig. 6a) and DJF (Fig. 6b). Figure 6a shows that the North Pacific High is dominant over both Regions A and B with anticyclonic circulation at 850 hPa in JJA. Although atmospheric environments and precipitation characteristics as organized precipitation systems are similar in Regions A and B, the details of atmospheric environments might differ. To extract typical atmospheric circulations associated with the precipitation events, a composite analysis for the 850-hPa horizontal winds is conducted (Fig. 7). Section 2.2 explained the details of the method. The target area is limited to the western parts of Regions A and B because they are too zonally broad to extract typical atmospheric circulations. Note that similar results can be confirmed for the eastern parts of Regions A and B (not shown). In addition to anomalous cyclonic circulations in the western part of Region A, Fig. 7a presents cyclonic anomalies over the southern part of Japan, which can be interpreted as the Baiu precipitation band of East Asia and extratropical cyclones around the band. Sampe and Xie (2010) show that the Baiu precipitation band extended eastward in the northwest Pacific Ocean, which might be related to the organized precipitation features over Region A, as found in this study.

In Region B over the subtropical region, the results in Figs. 5d and 5h suggest that the stratiform ratio over Region B was lower than that over Region A in JJA, indicating that precipitation systems over Region B consist of more convective precipitation than those over Region A. Yokoyama et al. (2017) suggest that

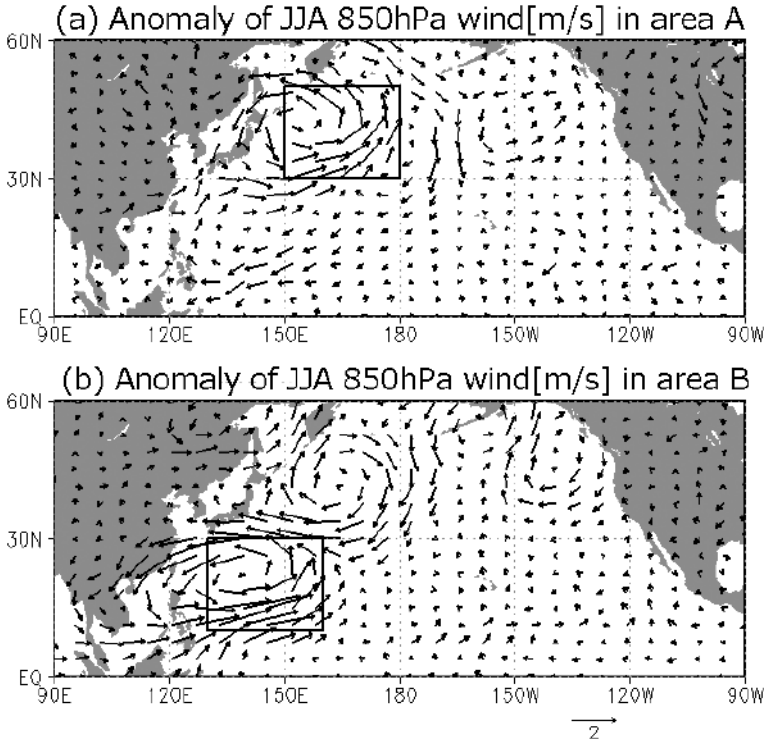


Fig. 7. Anomaly in composite analysis of horizontal winds at 850 hPa in mm $s^{-1}$ for the western part of (a) Region A and (b) Region B in JJA. The black open squares indicate the western part of Regions A and B.

the precipitation system with a stratiform ratio below 80 % was frequently observed in the subtropics, including Region B. It represented tropical mesoscale organized precipitation systems, such as mesoscale convective systems. Furthermore, tropical disturbances could be a contributor categorized as organized precipitation systems because they frequently develop around Region B in the northwest Pacific Ocean in July and August (Takahashi and Yasunari 2006). Figure 7b presents a large-scale cyclonic circulation that extends to the Philippines, which corresponds to the region where tropical disturbances, including tropical cyclones, are often observed. At the same time, Fig. 3a presents the same statistically significant $D_m$ signals off the eastern US coast, where hurricanes pass frequently. These climatological features support the proposed dominant precipitation regimes as organized systems.

### *5.2 Extratropical frontal systems over the mid-latitudes in DJF*

Contrary to the boreal summer over the northwest Pacific Ocean, the atmospheric circulations are quite different between the subtropical and mid-latitude regions in DJF. As for DJF in Region A, located to the east of a large continent, there is a storm track activity over the mid-latitudes (e.g., Blackmon et al. 1977). Figure 6b shows that Region A corresponds to the high-gradient region in SLP, and the Aleutian low stays in the northern part of Region A. Previous studies found that the size of the precipitation system over the mid-latitude ocean was large, especially in the winter (Liu and Zipser 2015).

Hamada et al. (2014) investigated the regional characteristics of extreme rainfall by using the 12-year TRMM dataset. They revealed that the frequency of extreme rainfall was high in autumn and winter over the oceans around 30°N. They suggested that the characteristics were related to extratropical frontal systems, which were the same as those in Region A in DJF in this study. The characteristics in Figs. 4a–d of high stratiform ratio with medium precipitation top heights correspond to the features of extratropical frontal systems. Looking back to Figs. 2f, 2h, and 3a, these signals can also be seen over the Atlantic Ocean in the northern hemisphere and throughout the south-

ern hemisphere (the signals in the southern hemisphere are opposite to those in the northern hemisphere, corresponding to winter). These results also support the dominance of extratropical frontal systems.

Dolan et al. (2018) suggested that large raindrops are formed originally from graupel or hail in ice-based precipitation and by melting at near surface, which is dominant in mid-latitudes. Although the results in this study are limited to cases for the liquid phase at near surface, ice particles could exist at upper levels above a clutter-free bottom. To check the existence of ice particles, the flagHIP is analyzed, and it is explained in Section 2.1. Figure 8 indicates the relative ratio of pixels with flagHIP to the total pixels with precipitation. It is found that the ratio of pixels with heavy ice precipitation is quite high over Region A, which means that ice particles exist at upper levels when $D_m$ near the surface is large in DJF.

Another possible factor for a large $D_m$ over the mid-latitudes in DJF is the growth of low-level raindrop (Kobayashi et al. 2018; Radhakrishna et al. 2020). Kobayashi et al. (2018) show the differences in reflectivity profiles for stratiform precipitation. The profiles frequently decreased from the melting level toward the surface in tropical oceans, whereas they increased in mid- and high-latitude oceans. They concluded that raindrops falling through the clouds collected the cloud droplets in the lower atmosphere, leading to the increasing raindrop size and radar reflectivity toward the surface. Radhakrishna et al. (2020) also suggest that the dominant lower-level hydrometeor growth due to the prevalence of moist atmosphere at low levels over the oceans resulted in larger $D_m$ values.

### *5.3 Shallow convective systems over subtropics in DJF*

Region B has the unique feature of the precipitation top height being the lowest and convective precipitation being dominant. Region B corresponds to the subtropical high and trade-wind region, as presented in Fig. 6b. The atmospheric lower-level stability in the trade-wind region is usually unstable enough to trigger convection. However, the trade-wind inversion suppresses convection to develop further, resulting in the dominance of low-level convective cumulus (Short and Nakamura 2000). In addition to the trade-wind cumulus, cumulus congestus is also prominent over the subtropics (Johnson et al. 1999; Takayabu et al. 2010). Thus, precipitation characteristics in Region B in DJF are consistent with the dominance of the shallow convective systems, such as cumulus and cumulus congestus.

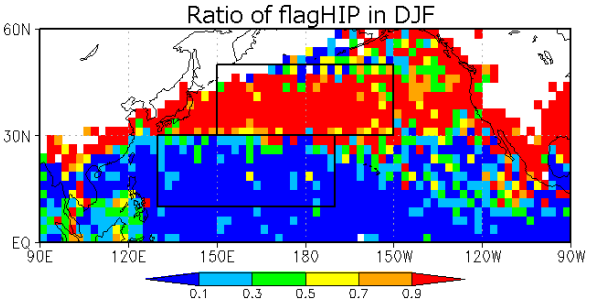


Fig. 8. 3-Month mean value of the ratio of pixels with heavy ice precipitation in DJF. The black open squares indicate Regions A and B, which are the same as in Fig. 3.

## 6. Pixel-by-pixel analysis of the $R$–$D_m$ relationship

Previous sections have shown that $D_m$ has seasonal variations associated with regional and seasonal changes in precipitation regimes. Over the mid-latitude region (Region A), $D_m$ is larger in DJF than in JJA with the change from an organized precipitation regime in JJA to an extratropical frontal regime in DJF. Conversely, $D_m$ is smaller in DJF than in JJA over the subtropical region (Region B) with the change from an organized precipitation regime in JJA to a shallow precipitation regime in DJF. Notably, the relationship between mean $R$ and mean $D_m$ does not follow the original pixel-based $R$–$D_m$ relationship used in the DPRL2 algorithm. As shown in the results, the seasonal variation in mean $R$ is insignificant, whereas that of $D_m$ is significant.

To elucidate whether the seasonal variation in $D_m$ is caused by the change in $R$ or by both $R$ and other precipitation characteristics, the pixel-by-pixel $R$–$D_m$ relationship at a clutter-free bottom is investigated using DPRL2 products. Two-dimensional histograms are calculated, as presented in Fig. 9. Noted that there is the unnatural separation of the stratiform/convective $R$–$D_m$ model, described by the dotted lines in Fig. 9, that is caused by the algorithm limitation. Although assuming that the $R$–$D_m$ relationship leads to artificial results, keep in mind that some samples are adjusted from the originally defined $R$–$D_m$ model through the change in $\varepsilon$. The range of $D_m$ becomes broader when log $R$ is within the narrow range of −0.5 to 1, which could cause the mean $D_m$ to vary even if mean $R$ exhibits no significant changes. Taking into consideration the frequency differences on the $R$–$D_m$ plane between JJA and DJF, Figs. 9c and 9f indicate that the dominant modes differ between seasons. The domi-

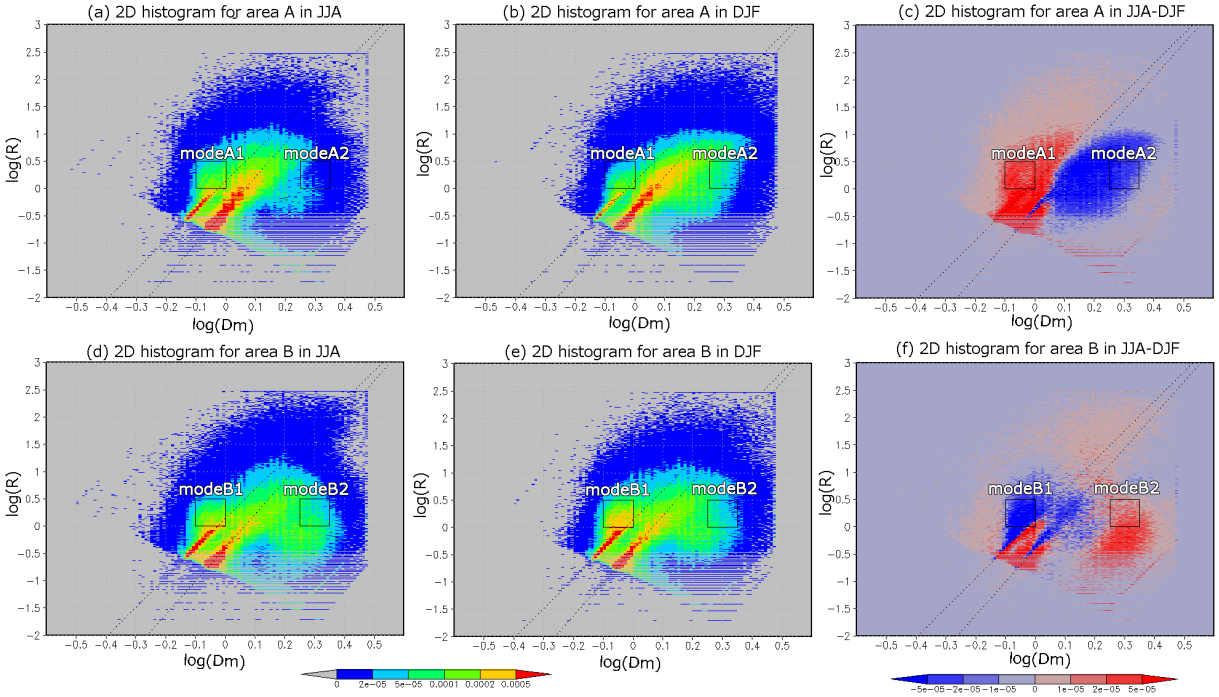


Fig. 9. Two-dimensional histogram of pixel-based $R$–$D_m$ relationship. Horizontal and vertical axes indicate log $D_m$ and log $R$, respectively. (a–c) are for Region A and (d–f) are for Region B. (a) and (d) are in JJA; (b) and (e) are in DJF. (c) and (f) are the differences between JJA and DJF (JJA minus DJF). The dotted lines in each panel indicate the $R$–$D_m$ base model assumed in the DPRL2 algorithm; the right and left dashed lines indicate the model for stratiform precipitation in Eq. (2) and convective precipitation in Eq. (3), respectively. The black open squares indicate the selected modes; left and right squares in Region A (a–c) indicate modes A1 and A2, and those in Region B (d–f) indicate modes B1 and B2, respectively.

nant modes are extracted as modes A1 and A2 over Region A (Figs. 9a–c) and B1 and B2 over Region B (Figs. 9d–f) by fixing the range of $R$ to discuss the differences in $D_m$. As for Region A in the mid-latitudes (Fig. 9c), mode A1 was dominant in JJA, whereas mode A2 was dominant in DJF. Conversely, mode B1 was dominant in DJF, whereas mode B2 was dominant in JJA over Region B in the subtropical region (Fig. 9f).

The result that mean $D_m$ could change even if mean $R$ is almost within the same range is consistent with the results and discussions in the previous section. To further investigate the differences for each mode, composite vertical profiles of $R$ within each mode and season are presented in Fig. 10. The vertical structures of $R$ differ in each mode and season even if the mean $R$ at the near surface is around 1.5–2 mm h$^{-1}$. It is noted again that all modes have the same range of $R$; however, modes A2 and B2 have a relatively larger $D_m$ ($0.25 < \log D_m < 0.35$) than modes A1 and B1 ($-0.1 <$ $\log D_m < 0$), respectively. Figure 10 shows that modes A2 and B2 with larger $D_m$ have relatively higher precipitation top heights compared with modes A1 and B1 in both JJA and DJF.

Regarding the 0°C level, the peak values of the 0°C level in JJA is 4–5 km and higher than those in DJF over Region A, whereas the peak values are almost 5 km in all modes in Region B. Comparing the differences between Regions A and B, the vertical profiles of $R$ with high relative frequency shown in warm colors are shallower in mode B1 than in mode A1 but deeper in mode B2 than in mode A2, despite the ranges of $R$ and $D_m$ being the same. This might depend on which precipitation systems are dominant in each season and each mode.

Focusing on the seasonal change in dominant precipitation systems over Region A in the mid-latitudes, mode A1 is more frequent in JJA when organized precipitation systems are dominant, whereas mode A2 is more frequent in DJF when extratropical frontal

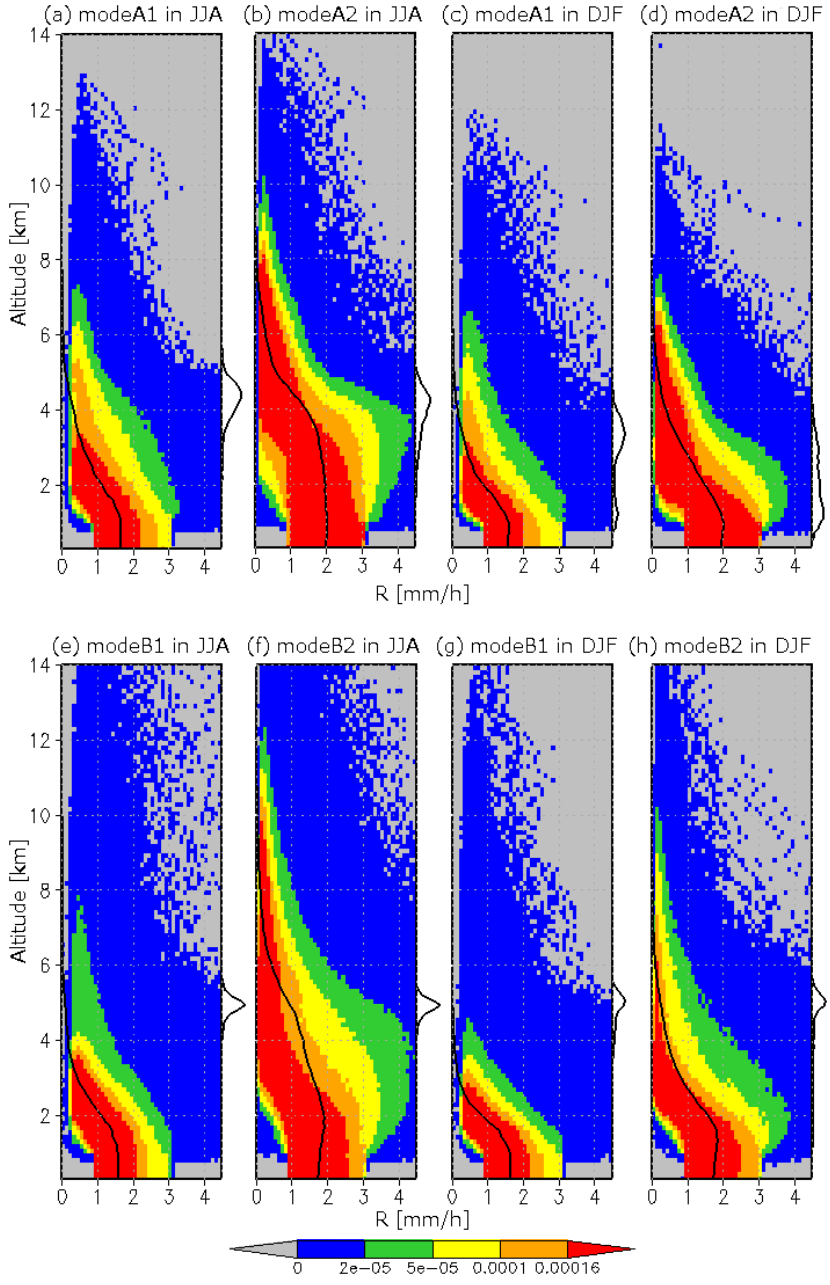


Fig. 10. Composite vertical profiles of $R$ for (a, c) mode A1, (b, d) mode A2, (e, g) mode B1, and (f, h) mode B2 in (a–b, e–f) JJA and in (c–d, g–h) DJF, respectively. The colors show relative frequency, superimposed by a solid line that indicates the mean for each height bin. The solid line along the right-hand axis of each panel indicates the histograms of 0°C levels.

systems are dominant, as presented in Fig. 9c. As compared with Figs 10a and 10d, the 0°C level is lower in mode A2 in DJF than in mode A1 in JJA. The lower 0°C level in mode A2 in DJF could provide more ice-based particles in the upper levels, which is consistent with the possible association between the existence of ice-based particles in the upper levels and larger $D_m$ melted at near surface in DJF over mid-latitudes. The results support the hypothesis that precipitation over a mid-latitude region, such as

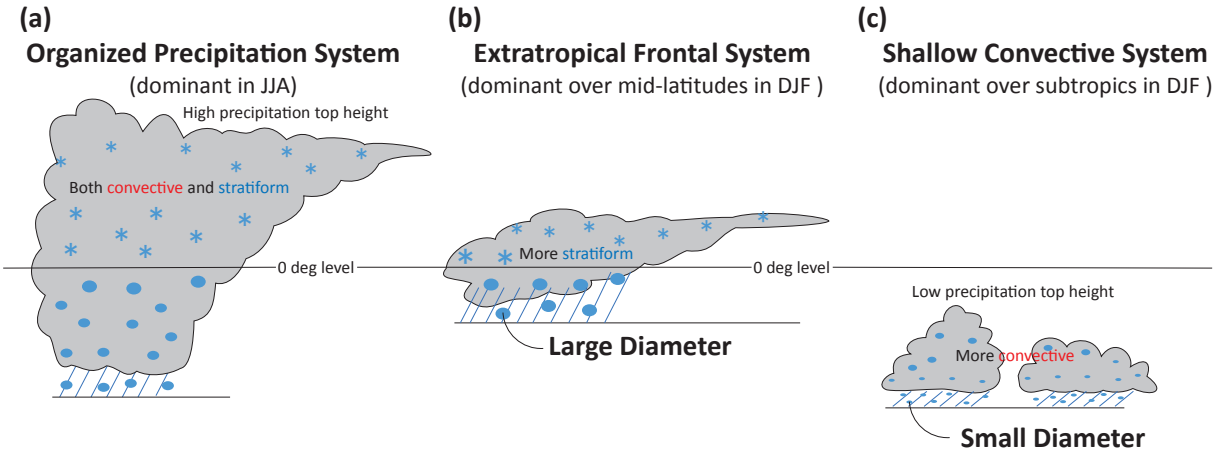


Fig. 11. Schematic diagram of three dominant precipitation systems discussed in this study: (a) organized precipitation system, (b) extratropical frontal system, and (c) shallow convective system.

Region A, could be often formed from ice processes (i.e., aggregation) in stratiform nimbostratus clouds falling into dry air, creating large values of $D_m$.

In the case of Region B over the subtropics, mode B2 is relatively more frequent in JJA when organized precipitation systems are dominant, whereas mode B1 is more frequent in DJF when shallow convective systems are dominant, as presented in Fig. 9f. Although the 0°C levels have almost the same values at 5 km, the vertical precipitation profiles are quite different. Precipitation top height is higher in mode B2 in JJA, which is consistent with the characteristics of organized precipitation systems. Regarding mode B1 in DJF, the precipitation top height of the mean vertical profile is below the 0°C level, which is the well-known precipitation characteristics of warm rain processes.

As shown by the pixel-based analysis, the variability of $D_m$ depends on $R$ and the changes in the dominant precipitation system, supporting the previous discussions. This could result in $R$ being nearly constant, despite the significant changes in $D_m$ that are related to the season or the specific region. However, it is difficult to identify the changes in $D_m$ regarding precipitation characteristics from those related to changes in $R$ and to deal with the artificial results caused by the $R$–$D_m$ relationship in the algorithm. Therefore, further investigation is required, and improvement of the algorithm is desired.

## 7. Conclusion

This study statistically analyzed 4 years of accumulated $D_m$ data from the DPRL2 Version 05 product to investigate the characteristics of global DSD and the relationship between characteristics of DSD and precipitation. New features of the GPM/DPR observations of DSD include the dual-frequency radar and the observed coverage of the mid-latitudes, compared with the predecessor TRMM/PR. This study found interesting characteristics of spatial distributions for the annual mean $D_m$ and the seasonal variations in $D_m$ through the change in the dominant precipitation systems by using the GPM/DPR observations.

The annual mean spatial distribution of $D_m$ is shown, and the values of $D_m$ are generally larger over land and smaller over the oceans. Over land, a larger $D_m$ corresponds to a larger $R$ in some areas. In the tropics and subtropics over the oceans, a larger $D_m$ also corresponds to a larger $R$, and $D_m$ is smaller over and around the eastern parts of the ocean with cold sea surface temperature and under the subtropical high. Over mid-latitude oceanic regions, $D_m$ is relatively larger, whereas $R$ is not so large, especially in the southern hemisphere.

$D_m$ varies seasonally with a change in $R$ over the Asian regions and the Amazon area over land and subtropical high and mid-latitudes over the oceans. Especially over the northern Pacific Ocean, $D_m$ is larger in the winter and smaller in the summer over the mid-latitude regions, and an opposite seasonal variation is observed over subtropical regions; the signals were statistically significant.

Further analysis is conducted focusing on the northwest Pacific Ocean by extracting two regions over the mid-latitude and subtropical regions (Regions A and B). Clear differences exist in dominant precipitation

systems with different precipitation characteristics over the two regions, with the variations in $D_m$. Figure 11 summarizes the results in this study. For both regions in JJA, the precipitation top heights are high, and there are both stratiform and convective precipitations. These characteristics are consistent with those of organized precipitation systems, such as the Baiu precipitation band of East Asia, extratropical cyclones around the band over the mid-latitudes, and tropical disturbances over the subtropics. For DJF over mid-latitudes, the stratiform ratio is high, but precipitation top heights are not as high as those for organized precipitation systems in JJA, corresponding to the features of extratropical frontal systems.

The results that the mean value of $R$ is not so large and ice particles exist in the upper level support the hypothesis that a large $D_m$ is related to not only a large $R$ but also the formation process of ice particles melting in the stratiform nimbostratus clouds falling into dry air. For DJF over the subtropics, a feature that precipitation top heights are the lowest and convective precipitation is dominant is confirmed. This result indicates that the shallow convective precipitation systems with trade-wind cumulus or cumulus congestus under the subtropical high are dominant in DJF, suggesting that $D_m$ varies seasonally and regionally, possibly regarding the changes in the dominant precipitation regimes.

To elucidate whether the seasonal variation in $D_m$ is caused by the change in $R$ or by both $R$ and other precipitation characteristics, the pixel-by-pixel $R$–$D_m$ relationship is investigated. It is found that most samples are around the originally assumed $R$–$D_m$ model that has a positive correlation; however, some samples are adjusted from the base model. The range of $D_m$ becomes broader from small values to large values, despite $R$ being within almost the same range around 1 mm $h^{-1}$, which could cause the variation in the mean $D_m$, even if mean $R$ does not change much. The dominant modes on the $R$–$D_m$ plane differ from season to season. Each dominant mode in season (JJA and DJF) and region (mid-latitudes and subtropics) has different vertical profiles of precipitation, which supported the discussions in the association between the regional and seasonal changes in $D_m$ and the dominant precipitation systems.

## Acknowledgments

The authors would like to express their sincere gratitude to Dr. Toshio Iguchi (National Aeronautics and Space Administration), Prof. Nobuhiro Takahashi (Nagoya University), Dr. Shinta Seto (Nagasaki University) for their constructive comments from algorithm insights. Prof. Kenji Nakamura (Dokkyo University) and Dr. Kaya Kanemaru (National Institute of Information and Communications Technology) provided valuable suggestions on this work. They also would like to thank three anonymous reviewers for their helpful comments.

## References

Akiyama, S., S. Shige, M. K. Yamamoto, and T. Iguchi, 2019: Heavy ice precipitation band in an oceanic extratropical cyclone observed by GPM/DPR: 1. A case study. *Geophys. Res. Lett.*, **46**, 7007–7014.

Blackmon, M. L., J. M. Wallace, N.-C. Lau, and S. L. Mullen, 1977: An observational study of the Northern Hemisphere wintertime circulation. *J. Atmos. Sci.*, **34**, 1040–1053.

Brandes, E. A., G. Zhang, and J. Vivekanandan, 2004: Comparison of polarimetric radar drop size distribution retrieval algorithms. *J. Atmos. Oceanic Technol.*, **21**, 584–598.

Bringi, V. N., V. Chandrasekar, J. Hubbert, E. Gorgucci, W. L. Randeu, and M. Schoenhuber, 2003: Raindrop size distribution in different climatic regimes from disdrometer and dual-polarized radar analysis. *J. Atmos. Sci.*, **60**, 354–365.

Collischonn, B., W. Collischonn, and C. E. M. Tucci, 2008: Daily hydrological modeling in the Amazon basin using TRMM rainfall estimates. *J. Hydrol.*, **360**, 207–216.

D'Adderio, L. P., G. Vulpiani, F. Porcù, A. Tokay, and R. Meneghini, 2018: Comparison of GPM Core Observatory and ground-based radar retrieval of mass-weighted mean raindrop diameter at midlatitude. *J. Hydrometeor.*, **19**, 1583–1598.

Dolan, B., B. Fuchs, S. A. Rutledge, E. A. Barnes, and E. J. Thompson, 2018: Primary modes of global drop size distributions. *J. Atmos. Sci.*, **75**, 1453–1476.

Hamada, A., Y. Murayama, and Y. N. Takayabu, 2014: Regional characteristics of extreme rainfall extracted from TRMM PR measurements. *J. Climate*, **27**, 8151–8169.

Hou, A. Y., R. K. Kakar, S. Neeck, A. A. Azarbarzin, C. D. Kummerow, M. Kojima, R. Oki, K. Nakamura, and T. Iguchi, 2014: The Global Precipitation Measurement mission. *Bull. Amer. Meteor. Soc.*, **95**, 701–722.

Houze, R. A., Jr., 1977: Structure and dynamics of a tropical squall–line system. *Mon. Wea. Rev.*, **105**, 1540–1567.

Iguchi, T., T. Kozu, R. Meneghini, J. Awaka, and K. Okamoto, 2000. Rain-profiling algorithm for the TRMM Precipitation Radar. *J. Appl. Meteor.*, **39**, 2038–2052.

Iguchi, T., T. Kozu, J. Kwiatkowski, R. Meneghini, J. Awaka, and K. Okamoto, 2009: Uncertainties in the rain profiling algorithm for the TRMM Precipitation Radar. *J. Meteor. Soc. Japan*, **87A**, 1–30.

Iguchi, T., S. Seto, R. Meneghini, N. Yoshida, J. Awaka, M. Le, V. Chandrasekar, and T. Kubota, 2017: *GPM/DPR level-2 algorithm theoretical basis document*. JAXA–NASA Tech. Rep., 81 pp. [Available at http://www.eorc.jaxa.jp/GPM/doc/algorithm/ATBD_DPR_201708_whole_1.pdf.]

Iguchi, T., N. Kawamoto, and R. Oki, 2018: Detection of intense ice precipitation with GPM/DPR. *J. Atmos. Oceanic Technol.*, **35**, 491–502.

IPCC, 2014: *Climate Change 2014: Synthesis Report. Contribution of Working Groups I, II and III to the Fifth Assessment Report of the Intergovernmental Panel on Climate Change*. The Core Writing Team, R. K., Pachauri, and L. Meyer (eds.), IPCC, Geneva, Switzerland, 151 pp.

Johnson, R. H., T. M. Rickenbach, S. A. Rutledge, P. E. Ciesielski, and W. H. Schubert, 1999: Trimodal characteristics of tropical convection. *J. Climate*, **12**, 2397–2418.

Kobayashi, K., S. Shige, and M. K. Yamamoto, 2018: Vertical gradient of stratiform radar reflectivity below the bright band from the Tropics to the extratropical latitudes seen by GPM. *Quart. J. Roy. Meteor. Soc.*, **144**, 165–175.

Kobayashi, S., Y. Ota, Y. Harada, A. Ebita, M. Moriya, H. Onoda, K. Onogi, H. Kamahori, C. Kobayashi, H. Endo, K. Miyaoka, and K. Takahashi, 2015: The JRA-55 Reanalysis: General specifications and basic characteristics. *J. Meteor. Soc. Japan*, **93**, 5–48.

Kojima, M., T. Miura, K. Furukawa, Y. Hyakusoku, T. Ishikiri, H. Kai, T. Iguchi, H. Hanado, and K. Nakagawa, 2012: Dual-frequency Precipitation Radar (DPR) development on the Global Precipitation Measurement (GPM) core observatory. *SPIE Proceedings, Vol. 8528: Earth Observing Missions and Sensors: Development, Implementation, and Characterization II*. Shimoda, H., X. Xiong, C. Cao, X. Gu, C. Kim, A. S. K. Kumar (eds.), SPIE, 234–243, doi:10.1117/12.976823.

Kozu, T., T. Kawanishi, H. Kuroiwa, M. Kojima, K. Oikawa, H. Kumagai, K. Okamoto, M. Okumura, H. Nakatsuka, and K. Nishikawa, 2001: Development of precipitation radar onboard the Tropical Rainfall Measuring Mission (TRMM) satellite. *IEEE Trans. Geosci. Remote Sens.*, **39**, 102–116.

Kozu, T., K. K. Reddy, S. Mori, M. Thurai, J. T. Ong, D. N. Rao, and T. Shimomai, 2006: Seasonal and diurnal variations of raindrop size distribution in Asian monsoon region. *J. Meteor. Soc. Japan*, **84A**, 195–209.

Kozu, T., T. Iguchi, T. Kubota, N. Yoshida, S. Seto, J. Kwiatkowski, and Y. N. Takayabu, 2009: Feasibility of raindrop size distribution parameter estimation with TRMM precipitation radar. *J. Meteor. Soc. Japan*, **87A**, 53–66.

Kruger, A., and W. F. Krajewski, 2002: Two-dimensional video disdrometer: A description. *J. Atmos. Oceanic Technol.*, **19**, 602–617.

Kummerow, C., W. Barnes, T. Kozu, J. Shiue, and J. Simpson, 1998: The Tropical Rainfall Measuring Mission (TRMM) sensor package. *J. Atmos. Oceanic Technol.*, **15**, 809–817.

Liu, C., and E. J. Zipser, 2015: The global distribution of largest, deepest, and most intense precipitation systems. *Geophys. Res. Lett.*, **42**, 3591–3595.

Löffler-Mang, M., and J. Joss, 2000: An optical disdrometer for measuring size and velocity of hydrometeors. *J. Atmos. Oceanic Technol.*, **17**, 130–139.

Marshall, J. S., and W. M. K. Palmer, 1948: The distribution of raindrops with size. *J. Meteor.*, **5**, 165–166.

Meneghini, R., H. Kim, L. Liao, J. A. Jones, and J. M. Kwiatkowski, 2015: An initial assessment of the surface reference technique applied to data from the dual-frequency precipitation radar (DPR) on the GPM satellite. *J. Atmos. Oceanic Technol.*, **32**, 2281–2296.

Ono, M., and H. G. Takahashi, 2016: Seasonal transition of precipitation characteristics associated with land surface conditions in and around Bangladesh. *J. Geophys. Res.: Atmos.*, **121**, 11190–11200.

Petersen, W. A., 2017: Use of polarimetric radar for evaluating GPM satellite-based retrievals of the rain drop size distribution. *Proceeding of AGU Fall Meeting 2017,* American Geophysical Union, A34A-01. [Available at https://ui.adsabs.harvard.edu/abs/2017AGUFM.A34A.01P.]

Petersen, W. A., P. N. Gatlin, D. B. Wolff, A. Tokay, and M. Grecu, 2018: A radar-based evaluation of GPM retrievals of the rain drop size distribution. *10th European Conference on Radar in Meteorology and Hydrology*, 1–6 July 2018, Ede-Wageningen, The Netherlands, Wageningen University and Research, doi:10.18174/454537.

Radhakrishna, B., K. Saikranthi, and T. N. Rao, 2020: Regional differences in raindrop size distribution within Indian subcontinent and adjoining seas as inferred from global precipitation measurement dual-frequency precipitation radar. *J. Meteor. Soc. Japan*, **98**, 573–584.

Sampe, T., and S. P. Xie, 2010: Large-scale dynamics of the meiyu-baiu rainband: Environmental forcing by the westerly jet. *J. Climate*, **23**, 113–134.

Seto, S., 2019: Evaluation of instantaneous rain rate estimates in DPR Version-06 products with rain gauge dataset over Japan. *Proc. IGARSS 2019*, Yokohama, Japan, 4473–4476, doi:10.1109/IGARSS.2019.8898795.

Seto, S., and T. Iguchi, 2015: Intercomparison of attenuation correction methods for the GPM dual-frequency precipitation radar. *J. Atmos. Oceanic Technol.*, **32**, 915–926.

Seto, S., T. Iguchi, and T. Oki, 2013: The basic performance of a precipitation retrieval algorithm for the Global Precipitation Measurement mission's single/dual-frequency radar measurements. *IEEE Trans. Geosci. Remote Sens.*, **51**, 5239–5251.

Seto, S., T. Shimozuma, T. Iguchi, and T. Kozu, 2016: Spatial and temporal variations of mass-weighted mean diameter estimated by GPM/DPR. *2016 IEEE International Geoscience and Remote Sensing Symposium (IGARSS)*, Beijing, 3938–3940.

Shige, S., T. Watanabe, H. Sasaki, T. Kubota, S. Kida, and K. Okamoto, 2008: Validation of western and eastern Pacific rainfall estimates from the TRMM PR using a radiative transfer model. *J. Geophys. Res.*, **113**, D15116, doi:10.1029/2007JD009002.

Short, D. A., and K. Nakamura, 2000: TRMM radar observations of shallow precipitation over the tropical oceans. *J. Climate*, **13**, 4107–4124.

Skofronick-Jackson, G., W. A. Petersen, W. Berg, C. Kidd, E. F. Stocker, D. B. Kirschbaum, R. Kakar, S. A. Braun, G. J. Huffman, T. Iguchi, P. E. Kirstetter, C. Kummerow, R. Meneghini, R. Oki, W. S. Olson, Y. N. Takayabu, K. Furukawa, and T. Wilheit, 2017: The Global Precipitation Measurement (GPM) mission for science and society. *Bull. Amer. Meteor. Soc.*, **98**, 1679–1695.

Straka, J. M., D. S. Zrnić, and A. V. Ryzhkov, 2000: Bulk hydrometeor classification and quantification using polarimetric radar data: Synthesis of relations. *J. Appl. Meteor.*, **39**, 1341–1372.

Takahashi, H. G., 2016: Seasonal and diurnal variations in rainfall characteristics over the tropical Asian monsoon region using TRMM-PR data. *SOLA*, **12A**, 22–27.

Takahashi, H. G., and T. Yasunari, 2006: A climatological monsoon break in rainfall over Indochina—A singularity in the seasonal march of the Asian summer monsoon. *J. Climate*, **19**, 1545–1556.

Takayabu, Y. N., 2008: Observing rainfall regimes using TRMM PR and LIS data. *GEWEX News*, **18**, 9–10.

Takayabu, Y. N., S. Shige, W. K. Tao, and N. Hirota, 2010: Shallow and deep latent heating modes over tropical oceans observed with TRMM PR spectral latent heating data. *J. Climate*, **23**, 2030–2046.

Testud, J., S. Oury, R. A. Black, P. Amayenc, and X. Dou, 2001: The concept of "normalized" distribution to describe raindrop spectra: A tool for cloud physics and cloud remote sensing. *J. Appl. Meteor.*, **40**, 1118–1140.

Ulbrich, C. W., 1983: Natural variations in the analytical form of the raindrop size distribution. *J. Climate Appl. Meteor.*, **22**, 1764–1775.

Wang, X., L. Zhang, and M. D. Moran, 2010: Uncertainty assessment of current size-resolved parameterizations for below-cloud particle scavenging by rain. *Atmos. Chem. Phys.*, **10**, 5685–5705.

Welch, B. L., 1938: The significance of the difference between two means when the population variances are unequal. *Biometrika*, **29**, 350–362.

Yokoyama, C., Y. N. Takayabu, and T. Horinouchi, 2017: Precipitation characteristics over East Asia in early summer: Effects of the subtropical jet and lower-tropospheric convective instability. *J. Climate*, **30**, 8127–8147.

Yokoyama, C., Y. N. Takayabu, O. Arakawa, and T. Ose, 2019: A study on future projections of precipitation characteristics around Japan in early summer combining GPM DPR observation and CMIP5 large-scale environments. *J. Climate*, **32**, 5251–5274.